Mon. Not. R. Astron. Soc. **363,** 79–92 (2005) doi:10.1111/j.1365-2966.2005.09405.x

A Very Small Array search for the extended Sunyaev–Zel'dovich effect in the Corona Borealis supercluster

Ricardo Génova-Santos,[1]★ José Alberto Rubiño-Martín,[1] Rafael Rebolo,[1]† Kieran Cleary,[2]‡ Rod D. Davies,[2] Richard J. Davis,[2] Clive Dickinson,[2]§ Nelson Falcón,[1,]‡‡ Keith Grainge,[3] Carlos M. Gutiérrez,[1] Michael P. Hobson,[3] Michael E. Jones,[3]¶ Rüdiger Kneissl,[3]‖ Katy Lancaster,[3]★★ Carmen P. Padilla-Torres,[1] Richard D. E. Saunders,[3] Paul F. Scott,[3] Angela C. Taylor[3]¶ and Robert A. Watson[2]††

[1]*Instituto de Astrofísica de Canarias, 38200 La Laguna, Tenerife, Canary Islands, Spain*
[2]*Jodrell Bank Observatory, University of Manchester, Macclesfield, Cheshire SK11 9DL*
[3]*Astrophysics Group, Cavendish Laboratory, University of Cambridge, Cambridge CB3 OHE*

Accepted 2005 July 6. Received 2005 May 5; in original form 2005 January 24

ABSTRACT

We present interferometric imaging at 33 GHz of the Corona Borealis supercluster, using the extended configuration of the Very Small Array. A total area of 24 deg^2 has been imaged, with an angular resolution of 11 arcmin and a sensitivity of 12 mJy beam^{-1}. The aim of these observations is to search for Sunyaev–Zel'dovich (SZ) detections from known clusters of galaxies in this supercluster and for a possible extended SZ decrement due to diffuse warm/hot gas in the intercluster medium. Hydrodynamical simulations suggest that a significant part of the missing baryons in the Local Universe may be located in superclusters.

The maps constructed from these observations have a significant contribution from primordial fluctuations. We measure negative flux values in the positions of the 10 richest clusters in the region. Collectively, this implies a 3.0σ detection of the SZ effect. For two of these clusters, A2061 and A2065, we find decrements of approximately 2σ each.

Our main result is the detection of two strong and resolved negative features at -70 ± 12 mJy beam^{-1} (-157 ± 27 μK) and -103 ± 10 mJy beam^{-1} (-230 ± 23 μK), respectively, located in a region with no known clusters, near the centre of the supercluster. We discuss their possible origins in terms of primordial cosmic microwave background (CMB) anisotropies and/or SZ signals related either to unknown clusters or to a diffuse extended warm/hot gas distribution. Our analyses have revealed that a primordial CMB fluctuation is a plausible explanation for the weaker feature (probability of 37.82 per cent). For the stronger one, neither primordial CMB (probability of 0.38 per cent) nor SZ can account alone for its size and total intensity. The most reasonable explanation, then, is a combination of both primordial CMB and SZ signal. Finally, we explore what characteristics would be required for a filamentary structure consisting of warm/hot diffuse gas in order to produce a significant contribution to such a spot taking into account the constraints set by X-ray data.

Key words: techniques: interferometric – galaxies: clusters: general – cosmic microwave background – cosmology: observations.

★E-mail: rgs@iac.es
†Consejo Superior de Investigaciones Científicas, Spain.
‡Present address: Jet Propulsion Laboratory, 4800 Oak Grove Drive, Pasadena, CA 91109, USA.
§Present address: California Institute of Technology, 1200 E. California Blvd., Pasadena, CA 91125, USA.
‡‡Departamento de Física, FACYT, Universidad de Carabobo, Venezuela.
¶Present address: Astrophysics Group, Department of Physics, Keble Road, Oxford OX1 3RH.
‖Present address: Department of Physics, University of California at Berkeley, CA 94720-7300, USA.
★★Present address: Astrophysics Group, University of Bristol, Tyndall Avenue, Bristol BS8 1TL.
††Present address: Instituto de Astrofísica de Canarias, 38200 La Laguna, Tenerife, Spain.

1 INTRODUCTION

The mean baryon density of the Universe is one of the most relevant cosmological parameters, as it influences baryonic structures on all scales, from the abundances of primordial nuclei to the large-scale distribution of galaxies and intergalactic gas. Indeed, its value is also a prediction of the standard big bang model that may be tested observationally. The calculation of the primeval abundances of light elements, such as deuterium, combined with standard big bang nucleosynthesis, allows a very precise determination of this parameter for standard models (Burles, Nollett & Turner 2001): $\Omega_{\rm B} = (0.020 \pm 0.002)\, h^{-2} = 0.038 \pm 0.004$, where here $h \equiv h_{100} = H_0/100\,{\rm km\,s^{-1}\,Mpc^{-1}} = 0.73$ is adopted for the last term. Likewise Rauch et al. (1997) derive a lower limit $\Omega_{\rm B} = 0.021\, h^{-2} = 0.042$ for a ΛCDM model from observations of the Lyα forest absorption in a selected sample of seven high-resolution quasar spectra at $z = 2$. More recently, the best-fitting cosmological model to the first-year *WMAP* data release also gives a value $\Omega_{\rm B} = (0.0224 \pm 0.0009)\, h^{-2} = 0.044 \pm 0.002$ (Spergel et al. 2003), while the recent Very Small Array (VSA) results give $\Omega_{\rm B} = (0.0234^{+0.0012}_{-0.0014})\, h^{-2} = 0.0464^{+0.0024}_{-0.0028}$ (Rebolo et al. 2004).

In principle, the consistency between these three completely independent methods of estimating the baryon density is straightforward, but at $z = 0$ in the present-day Universe, the sum over all the well-observed components gives a considerably smaller value. Indeed, Fukugita, Hogan & Peebles (1998) made an estimate of the global budget of baryons in all known states, namely the different kinds of stars, the atomic and molecular gas, and the plasma in galaxy clusters and in groups. They infer a value $\Omega_{\rm B} = (0.010 \pm 0.003)\, h^{-2} = 0.020 \pm 0.007$.

Thus, if no serious errors have been made in the theoretical estimates, which seems unlikely given the agreement between the different methods, it seems that most of the baryons are yet to be detected in the present-day Universe. This is the well-known 'baryon problem'.

One of the most important hypotheses related to this hidden matter is based upon hydrodynamical simulations (Cen & Ostriker 1999; Davé et al. 2001), which predict the formation at low redshift ($z < 1$) of a very diffuse gas phase with temperatures $10^5 < T < 10^7$ K, which is neither low enough to have permitted condensations into stars or to form cool galactic gas, nor as high as that of the hot gas present in galaxy clusters. Such low-density gas could account for a substantial fraction of the missing baryons, and according to these simulations it should be distributed in large-scale sheet-like structures and filaments connecting clusters of galaxies, due to the infall of baryonic matter into previously formed dark matter filaments. Moreover, this amount of gas would not violate the constraints on the spectral distortions of the cosmic microwave background (CMB). It constitutes what is known as the 'warm/hot intergalactic medium' (WHIM) and would be observed in the soft X-ray band. The detection of its radiation could be obscured by the presence of many galactic foregrounds and by extragalactic contributions from groups of galaxies, clusters or active galactic nuclei (AGNs). Nevertheless, several attempts in recent years have been made to detect it, and some detections have been claimed, either by studying the correlation between the observed soft X-ray structures and selected galaxy overdense regions (Scharf et al. 2000; Zappacosta et al. 2002) or by detecting a soft X-ray excess in clusters of galaxies (Finoguenov, Briel & Henry 2003), or in their proximity (Briel & Henry 1995; Tittley & Henriksen 2001; Sołtan, Freyberg & Hasinger 2002).

As indicated by Cen & Ostriker (1999), both X-ray emission and the thermal Sunyaev–Zel'dovich (SZ) effect can be cross-correlated with galaxy or galaxy cluster catalogues to search for the missing baryons. The SZ effect typically originates from the richest clusters of galaxies that contain extended atmospheres of hot gas ($k_{\rm B}T_{\rm e} \sim 10$ keV). However, there may be other objects that could also produce a detectable SZ signal, such as superclusters of galaxies, where, even though low baryon overdensities are expected, pathlengths may be long. Thus, a significant SZ effect could build up, since the effect is proportional to the line-of-sight integral of the electron density (Birkinshaw 1999). Also, it is reasonable to look at superclusters as optimal regions for the detection of WHIM, since simulations show that this gas should be distributed in filamentary structures extending over several tens of megaparsecs and connecting clusters of galaxies. In fact, Molnar & Birkinshaw (1998) looked in the *COBE*-DMR data in the region of the Shapley supercluster, but found no clear evidence of an extended SZ effect, and therefore set an upper limit of $\lesssim -100\,\mu$K on the gas temperature. On the other hand, several studies have been carried out, not by searching in selected overdense regions, but by trying to obtain a statistical SZ detection from intra-supercluster (ISC) gas from analyses of the whole sky, first using the *COBE*-DMR data (Banday et al. 1996) and, more recently, the first release of *WMAP* data (Fosalba, Gaztañaga & Castander 2003; Hernández-Monteagudo & Rubiño-Martín 2004; Myers et al. 2004; Hernández-Monteagudo, Genova-Santos & Atrio-Barandela 2004). This is mainly carried out by correlating CMB maps with templates built from galaxy or galaxy cluster catalogues.

In this study we concentrate on the Corona Borealis supercluster (CrB-SC). This supercluster does not contain high flux density radio sources that may inhibit SZ measurements. The supercluster members have relatively high X-ray fluxes (Ebeling et al. 1998, 2000), which suggests that detectable SZ effects could build up. Also, the angular size of the supercluster core is suitable for mosaicked observations with the VSA extended array, which has a primary beam full width at half-maximum (FWHM) of 2.1°. Taking these factors into account, we selected this supercluster as the most interesting object of its type within the region of sky observable by the VSA (which has a declination coverage of $\approx -7°$ to $+63°$).

In Section 2 we present a general description of the CrB-SC and summarize previous observational work. Section 3 includes an overview of the VSA interferometer and explains the data reduction and the map-making procedure. In Section 4 we discuss the SZ effects from the individual clusters in the region and the possible causes of the two observed negative features. Conclusions are presented in Section 5.

2 THE CORONA BOREALIS SUPERCLUSTER

The CrB-SC is one of the most prominent examples of superclustering in the northern sky. Shane & Wirtanen (1954), after counting galaxies on the Lick Observatory photographic plates, were the first to remark upon the extraordinary cloud of galaxies that constitute the supercluster, and later Abell (1958) noted the presence of this concentration of clusters of galaxies, including it in his catalogue of second-order clusters. Depending on author, the number of clusters belonging to this SC ranges from six to eight (Postman, Geller & Huchra 1988; Small, Sargent & Hamilton 1997), but we will focus on the classification given in the Einasto et al. (2001) catalogue, according to which the CrB-SC includes eight clusters, around the position RA $= 15^{\rm h}25^{\rm m}16\overset{\rm s}{.}2$, Dec. $= +29°31'30''$, at a redshift $z \approx 0.07$. These clusters are listed in Table 1, along with their characteristics. Six of these (A2061, A2065, A2067, A2079, A2089 and A2092) are located in the core of the SC, in an $\approx 3 \times 3$ deg^2

Table 1. Basic data for the clusters. The coordinates are the optical centre of each cluster. The last two columns show the predicted flux that would be observed by the VSA for those clusters with X-ray measurements (labelled 'pred', see Section 4.1 for details), and the measured value in our final maps (labelled 'VSA'). The error bars contain the thermal noise (σ_n), the average primordial CMB (which has been computed to be $\sigma_{CMB} \approx 19\,mJy\,beam^{-1}$) and the residual sources ($\sigma_{sour} \approx 6\,mJy\,beam^{-1}$) added in quadrature. Clusters from A2019 to A2124 belong to CrB-SC, whereas A2069 and A2073 are located in the same region but at a larger distance along the line of sight.

Cluster	RA[a] (J2000)	Dec.[a] (J2000)	z[a]	L_X(0.1–2.4 keV) ($10^{44}\,h_{50}^{-2}\,erg^{-1}$)[b]	T_e (keV)	ΔS_ν^{pred} (mJy beam^{-1})	ΔS_ν^{VSA} (mJy beam^{-1})
A2019	15 02 57.2	+27 11 17	0.0807				-2.6 ± 24.5
A2061	15 21 15.3	+30 39 17	0.0784	3.95[c]	5.6[c]	−54.7	-53.8 ± 27.4
A2065	15 22 42.6	+27 43 21	0.0726	4.94[c]	8.4[c]	−61.7	-42.8 ± 23.4
A2067	15 23 14.8	+30 54 23	0.0739	0.86[d]	3.1[d]	−27.7	-26.5 ± 27.4
SCL-158	15 25 16.2	+29 31 30					
A2079	15 28 04.7	+28 52 40	0.0690				-6.7 ± 22.6
A2089	15 32 41.3	+28 00 56	0.0731				-28.9 ± 27.9
A2092	15 33 19.4	+31 08 58	0.0669				-21.0 ± 28.5
A2124	15 44 59.3	+36 03 40	0.0656	1.35[c]	3.7[c]	−44.3	-19.4 ± 29.2
A2069	15 23 57.9	+29 53 26	0.1160	8.92[c]	7.9[c]	−57.1	-15.2 ± 27.4
A2073	15 25 41.5	+28 24 32	0.1717	3.74[d]	5.6[d]	−29.9	-33.4 ± 22.6

[a]NASA Extragalactic Database. [b]Note the use of $h_{50} = H_0/50\,km\,s^{-1}\,Mpc^{-1}$. [c]Ebeling et al. (1998). [d]Ebeling et al. (2000).

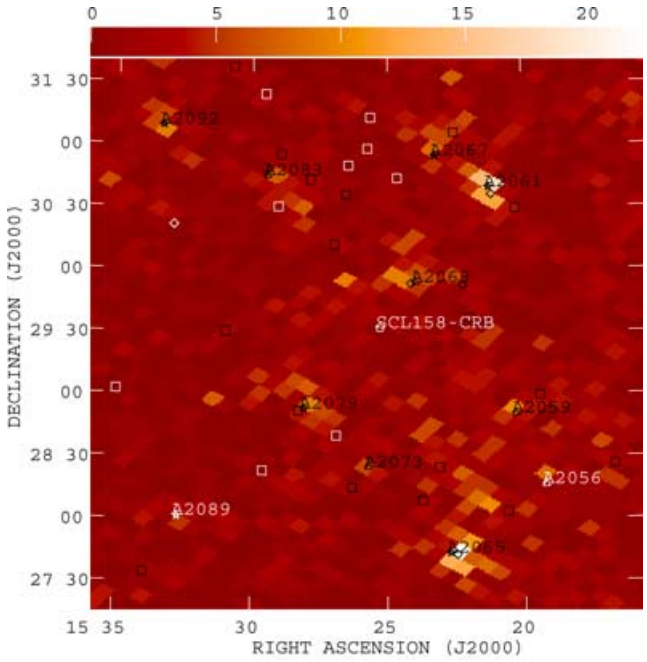

Figure 1. Spatial distribution of the galaxy clusters present in the CrB-SC core region. The centre of the supercluster, as reported by Einasto et al. (2001), is indicated with a pentagon. Five-pointed stars, triangles, squares and diamonds indicate respectively the positions of the CrB-SC clusters, other Abell clusters, Zwicky clusters and clusters present in other catalogues (their coordinates are taken from the NASA Extragalactic Database). The background shows the projected galaxy density in a pixelization with a resolution of ≈7 arcmin. It was built by assigning to each pixel a value equal to the number of galaxies of the Two Micron All Sky Survey (2MASS) Extended Source Catalogue (Jarrett et al. 2003) contained in the pixel.

region, while there are two others (A2019 and A2124) at an angular distance of ≈2.5° from the core. Einasto et al. (2001) include only A2061 and A2065 as X-ray-emitting clusters. There are four other Abell clusters (A2056, A2005, A2022 and A2122) in this region at redshifts around $z \approx 0.07$, two (A2069 and A2083) at $z \approx 0.11$, and another two (A2059 and A2073) that are even more distant. There are also several Zwicky clusters, but without redshift measurements. The spatial distribution of these clusters can be seen in Fig. 1.

The first dynamical study of the CrB-SC was carried out by Postman et al. (1988), through the study of a sample of 1555 galaxies in the vicinity of Abell clusters. They report 97 new redshift measurements over the previous 85. They conclude that the masses of all clusters in the core of the CrB-SC lie in the range $(1.5–8.9) \times 10^{14}\,M_\odot$, while the mass of the SC is approximately $\approx 8.2 \times 10^{15}\,M_\odot$, which is probably enough to bind the system. They proved also that the dynamical time-scales are comparable with the Hubble time, making it unlikely that the system could be virialized, as one might expect. This work was extended by Small et al. (1998) by increasing the number of galaxies with known redshifts to 528. They quote a value for the mass of the supercluster of $(3–8) \times 10^{16}\,h^{-1}\,M_\odot$, a value slightly higher than the previous one. This is because Postman et al. (1988) made the assumption that the mass-to-light ratio in the CrB-SC is the same as in the richest Abell clusters, and they used a supercluster volume three times smaller. They remark that almost one-third of the galaxies in the region are not linked to any Abell cluster, and also emphasize the great contribution to the projected surface density of galaxies of the background cluster A2069 and its surrounding galaxies, located at a redshift $z \approx 0.11$, suggesting the existence of the so-called 'A2069 supercluster'. On the other hand, Marini et al. (2004) have analysed the *BeppoSax* X-ray data in a search for evidence of a merging signature between the pairs of cluster candidates in the region of CrB-SC A2061–A2067 and A2122–A2124. They find no clear evidence of interaction, but detect a candidate shock inside A2061.

3 OBSERVATIONS AND DATA REDUCTION

3.1 Observations with the VSA interferometer

The Very Small Array (VSA) is a 14-element heterodyne interferometric array, tunable between 26 and 36 GHz with a 1.5 GHz bandwidth and a system temperature of approximately 35 K. It is located at an altitude of 2400 m at the Teide Observatory in Tenerife. For this study, the observing frequency was set at 33 GHz, and we used the extended configuration, which uses conical corrugated horn

Table 2. Summary of the observations with the VSA. We list the central coordinate of the 11 pointings, the total observation time, the integration time and the thermal noise achieved for each map (computed from the map far away from the primary beam FWHM).

Pointing	RA (J2000)	Dec. (J2000)	$T_{\rm obs}$ (h)	$T_{\rm int}$ (h)	Thermal noise (mJy beam^{-1})
CrB-A	15 23 12.00	+28 06 00.0	54	50	12.4
CrB-B	15 27 48.00	+29 24 00.0	70	70	10.8
CrB-C	15 22 48.00	+30 21 00.0	33	33	18.9
CrB-D	15 32 00.00	+30 45 00.0	19	19	20.5
CrB-E	15 32 00.00	+28 18 00.0	22	22	19.7
CrB-F	15 02 57.20	+27 11 17.3	47	43	14.4
CrB-G	15 45 00.00	+36 03 57.6	19	19	21.4
CrB-H	15 23 00.00	+29 13 30.0	167	130	10.2
CrB-I	15 27 24.00	+30 33 00.0	56	41	18.6
CrB-J	15 32 00.00	+29 31 30.0	55	39	18.9
CrB-K	15 28 00.00	+28 12 00.0	41	33	20.3

antennae with 322 mm apertures, and has a primary beam FWHM of 2.1°, and a synthesized beam FWHM ≈ 11 arcmin at the observing frequency. For a detailed description of the instrument, see e.g. Watson et al. (2003).

Situated next to the main array is a two-element interferometer, which consists of two 3.7-m diameter dishes with a north–south baseline of 9 m, giving a resolution of 4 arcmin in a 9 arcmin field. This interferometer is used for source subtraction (SS), monitoring radio sources simultaneously with the main array observations, as described in Taylor et al. (2003). This strategy neatly copes with the additional problem of source variability.

The observations were carried out during the period 2003 spring–2004 summer, although most of the data were taken in the first months, while the last months were used only to improve the noise levels in those fields with a poorer signal-to-noise ratio, and to obtain a better measurement of the fluxes of some of the radio sources. Initially, we observed five individual patches covering the interesting central regions of the supercluster, plus two additional pointings separate from the main mosaic and centred on clusters A2019 and A2124. We later added four more pointings to improve the coverage of the supercluster core. These observations are described in Table 2. Each daily observation was approximately 4 h in duration. We dedicated between five (for CrB-D and CrB-G) and 37 (for CrB-H) days to each pointing. We quote both total observation and integration times, the latter indicating the data retained after flagging (for instance, periods of bad weather).

3.2 Calibration and data reduction

The primary calibrator for the VSA is Jupiter. The flux scale is transferred to other calibration sources: Tau A (the Crab nebula) and Cas A, which are observed daily. A detailed description of the VSA calibration process is presented in Watson et al. (2003), whereas in Grainge et al. (2003) and Dickinson et al. (2004) are remarked the specifications adopted for the VSA extended configuration.

In the first VSA studies (e.g. Watson et al. 2003; Grainge et al. 2003) the calibration scale was based on the effective temperature of Jupiter given by Mason et al. (1999), which extrapolated to 33 GHz is $T_{\rm Jup} = 153 \pm 5$ K (3 per cent accuracy in temperature). In the most recent VSA published data (Dickinson et al. 2004), we rescale our results using the Jupiter temperature as derived from the *WMAP* first-year data: $T_{\rm Jup} = 146.6 \pm 2.0$ K (Page et al. 2003), which agrees with the Mason et al. (1999) value at 1σ level, but reduces the calibration error from 3 to 1.5 per cent in temperature terms (from 6 to 3 per cent in the power spectrum). In this paper we have also rescaled the Jupiter temperature to the *WMAP* value, which is the most accurate value published to date.

The correlated signal from each of 91 VSA baselines is processed as described in Watson et al. (2003) and Grainge et al. (2003), and the data checks so described are also applied.

3.3 Source subtraction

In order to remove the effect of radio sources from the data, we followed a slightly different approach to that considered for the primordial CMB fields (see Cleary et al. 2005). For those fields, the Ryle Telescope (RT) was used to identify all the sources above a given threshold at 15 GHz [see Taylor et al. (2003) and Grainge et al. (2003) for the compact and extended arrays, respectively]. Using this catalogue, the source subtraction baseline monitored all these sources in real time, and the derived fluxes were subtracted from the VSA main array data. However, for the present study a complete scanning of the region with the RT was not available because of observing time constraints, so in order to build a source catalogue in the region, we proceeded as follows. All the sources in the NVSS–1.4 GHz (Condon et al. 1998) and GB6–4.85 GHz (Gregory et al. 1996) catalogues closer than 2° from each pointing position were identified. Using the fluxes from these catalogues, the inferred spectral index between the respective frequencies was used to extrapolate the flux to 33 GHz. Finally, all sources with predicted fluxes above 20 mJy at 33 GHz were monitored using the SS baseline. The flux threshold was chosen according to the requirements for the primordial CMB fields, but, as we shall see below, for the purposes of this paper this limit can be relaxed.

Source positions were assigned according to the coordinates in the GB6 catalogue. This catalogue has a lower angular resolution (FWHM ≈ 3.5 arcmin) than the NVSS (FWHM ≈ 45 arcsec), so multiple sources in NVSS could be associated with a single entry in the GB6 catalogue. This was taken into account when computing the spectral index for each source: the adopted flux at the NVSS frequency was derived using the GB6 resolution, combining all sources in NVSS that correspond to a given entry in the GB6 catalogue (i.e. for each GB6 source, we found all the NVSS sources closer than 5 arcmin, applied the primary beam correction, and summed the corrected fluxes).

Taking into account that the sensitivity of the GB6 catalogue is 18 mJy at 4.85 GHz, together with a maximum value of the rising spectral index between 1.4 and 33 GHz (e.g. Mason et al. 1999) of $\alpha = -0.5$ ($S \propto \nu^{-\alpha}$), we are confident that we have measured all radio sources with fluxes above ≈50 mJy at 33 GHz. Nevertheless, we appreciate that sources with inverted spectra and higher fluxes may exist, and identify four compact features at the $3\sigma_{\rm n}$ level ($\sigma_{\rm n}$ being the standard deviation of the thermal noise) in our maps of the CrB-SC region. We suspected that these may be radio sources not picked up by our strategy, but source subtractor observations suggest otherwise. No sources with detectable fluxes (i.e. $S > 20$ mJy at the 2σ level) were found at those positions.

A total of 74 sources closer than 2° to any pointing were found to have an extrapolated flux greater than 20 mJy at 33 GHz, and of these, only 25 had a measured flux with the source subtractor greater than 50 mJy. In Table 3 we present the final list of identified sources with measured fluxes greater than 50 mJy at 33 GHz. These values were used to carry out the source subtraction.

It should be noted that this flux limit is larger than that used for the analyses of the primordial CMB fields with the extended VSA array.

Table 3. List of all the radio sources with measured fluxes at 33 GHz above 50 mJy. We quote the extrapolated flux at 33 GHz, and the estimated flux at 33 GHz using the SS observations, which have been used to subtract the sources from the data.

	Name	RA (J2000)	Dec. (J2000)	Extrapolated flux by NVSS-GB6 at 33 GHz (mJy)	Measured flux by the SS at 33 GHz (mJy)
CrB-F	1459+2708	14 59 39.60	27 08 16.0	83	132 ± 12
	1504+2854	15 04 27.30	28 54 25.0	76	193 ± 14
	1509+2642	15 09 39.10	26 42 45.0	39	58 ± 10
Mosaic	1514+2931	15 14 20.90	29 31 09.0	104	95 ± 6
	1514+2855	15 14 40.30	28 55 39.0	72	63 ± 8
	1514+2943	15 14 03.70	29 43 21.0	33	50 ± 13
	1521+3115	15 21 01.80	31 15 50.0	196	69 ± 43
	1522+3144	15 22 09.50	31 44 18.0	243	296 ± 7
	1522+2808	15 22 48.90	28 08 51.0	133	97 ± 5
	1527+3115	15 27 18.20	31 15 14.0	294	157 ± 6
	1528+3157	15 28 52.60	31 57 34.0	75	98 ± 7
	1529+3225	15 29 38.70	32 25 23.0	60	84 ± 38
	1531+2819	15 31 21.40	28 19 26.0	30	58 ± 9
	1532+2919	15 32 20.20	29 19 40.0	71	51 ± 12
	1535+3126	15 35 58.90	31 26 25.0	47	53 ± 5
	1537+2648	15 37 06.40	26 48 24.0	23	56 ± 18
	1539+3103	15 39 15.90	31 03 59.0	107	86 ± 15
	1539+2744	15 39 38.80	27 44 33.0	244	218 ± 10
CrB-G	1538+3557	15 38 57.40	35 57 09.0	37	54 ± 12
	1540+3538	15 40 31.70	35 38 26.0	24	52 ± 16
	1544+3713	15 44 44.70	37 13 22.0	25	50 ± 11
	1546+3631	15 46 07.60	36 31 07.0	26	51 ± 18
	1546+3644	15 46 38.30	36 44 30.0	44	59 ± 15
	1547+3518	15 47 51.70	35 18 59.0	87	77 ± 12
	1552+3716	15 52 05.30	37 16 05.0	47	50 ± 18

For that study, we used a flux limit of 20 mJy, which guarantees that the residual contribution from unsubtracted sources is less than the flux sensitivity (Grainge et al. 2003; Dickinson et al. 2004; Cleary et al. 2005), and this could be achieved thanks to the RT survey at 15 GHz. However, as we shall see below (Section 4.2), the main result of this paper is the detection of two anomalous cold regions with the VSA in the CrB-SC region, which seem difficult to explain as primordial CMB features. We took our list of extrapolated fluxes and used the values to determine the effects on our measurements of the cold spots. We found that the individual effect of any one source was sufficient only to affect our measurements by less than 2 per cent, and that the collective effect of all sources would cause effects of 1.3 and 3.2 per cent, respectively, in the two spots. This latter error is only twice the calibration error. Thus for the purposes of this paper [in contrast with the VSA power spectrum measurements, where more stringent source constraints were required (Scott et al. 2003; Grainge et al. 2003; Dickinson et al. 2004)], our source subtraction limit of 50 mJy is sufficient.

In any case, an estimate of the confusion noise due to unresolved sources below our source subtraction threshold can be made using the best-fitting power-law model obtained from the source count above ≈50 mJy (see fluxes in Table 3),

$$n(S) = (17.6 \pm 2.3) \left(\frac{S}{70\ \mathrm{mJy}} \right)^{-2.28 \pm 0.83} \quad \mathrm{mJy}^{-1}\ \mathrm{sr}^{-1}. \qquad (1)$$

Note that this fit has a slope compatible with that of the model presented in Cleary et al. (2005), which was obtained using the source count from the VSA primordial CMB observations. However, the amplitude in our case is a factor of ≈1.7 larger. This is as expected since there may be a higher density of radio sources in the supercluster due to the presence of sources associated with the member clusters. Indeed, the model of Cleary et al. (2005) predicts just 15 radio sources above 50 mJy in our region of observation, whereas we find 25. Using the model described by equation (1), we estimate that the residual sources may introduce a confusion noise $\sigma_{\mathrm{sour}} = 7.3\,\mathrm{mJy\,beam}^{-1}$. Note, however, that this result may overestimate the real confusion noise in the regions far away from the CrB-SC clusters, where the source count should be described by the model given in Cleary et al. (2005).

To conclude this section, we also report a problem that was detected during a late stage in the data processing, related to SS measurements. Since the source subtractor continually slews between pointed observations of point sources inside the observed VSA fields, the phase stability of the system has to be checked several times during an observing run, as described in Watson et al. (2003). To this end, we observe several interleaved strong calibration sources close to the considered region on the sky in order to track the phase stability of the system properly. We found that one of the calibration sources used in the CrB-SC central mosaic was not as bright as predicted by the extrapolation and hence was not bright enough to produce a sufficiently accurate determination of the phase. Using Monte Carlo simulations with the known calibrator flux and the sensitivity of the measurement, it is easy to show that a weak calibration source produces an average underestimate of the source flux. From these simulations, we could try to correct all the flux measurements, but this would require us to make an assumption about the variability of each source. Instead, we decided to use a new estimator of the flux of the source that does not require phase calibration.

Let us introduce the estimator $E[S^2] = V_{\mathrm{R}}^2 + V_{\mathrm{I}}^2 - 2\sigma_{\mathrm{n}}^2$, where S is the flux of the source we are measuring, V_{R} and V_{I} the real and imaginary parts of the visibility, and σ_{n} the statistical noise

of each measurement. By construction, this estimator is unbiased ($\langle E[S^2]\rangle = \langle S^2\rangle$) and is not sensitive to phase error of the instrument. If the noise is Gaussian, then E is distributed as a (displaced) χ^2 with two degrees of freedom. However, we must note that, for our purposes, this estimator can only be used for the case of non-variable sources, because it provides $\langle S^2\rangle$ during the whole period of observation, and not $\langle S\rangle$, which is the quantity we are interested in. Thus, we finally decided to use the estimator $E' = \sqrt{E}$ to derive the fluxes. This estimator is obviously defined only for positive values of E and in principle is biased to high values of the flux if the signal-to-noise ratio of the measurement is small. This bias was computed and we find that, for the flux sensitivity of the instrument, it is significant only for values of the flux smaller than 50 mJy. However, we have reduced this bias by averaging the square estimator, E, between adjacent measurements of the same source to get a positive value prior to application of the square root. Summarizing, even if we do not have an accurate determination of the phase of the instrument at the time of the observation for some of the sources, their fluxes can be recovered from our measurements using this new estimator, although the error bar on the final measurement will be larger than the one obtained with the standard procedure.

In addition, and as a consistency check, we re-observed the strongest sources in the mosaic, with estimated fluxes above $\approx$60 mJy, but now using an appropriate calibrator. A variability study was then applied to all these sources following the same criteria as in Cleary et al. (2005), and variable sources were identified. Only five sources were found to be variable. For non-variable sources, the new flux was directly compared to our previous determination to check that our flux values are robust. Final values for the fluxes are presented in Table 3.

3.4 VSA maps

Daily observations are calibrated and reduced as described in Section 3.2 (and references therein) and are held as visibility files, which contain the real and imaginary parts measured at each *uv*-position together with the associated rms noise level. These files are loaded individually into AIPS (Greisen 1994), where the map-making process is carried out using standard tasks. The individual visibility files are stacked. Each of these stacks contains typically $\simeq$300 000 visibility points, each one averaged over 64 s. The source subtraction is implemented in the aperture plane using AIPS task UVSUB, and then the maps for each individual pointing are produced. We used natural weighting, the most appropriate in this case since it produces the highest sensitivity and given that the sampling of the aperture plane is practically uniform. From the nine central pointings we produced the mosaicked map using standard AIPS tasks. Tasks LTESS and STESS were used to make a map in primary beam-corrected units, followed by a sensitivity map, which is practically uniform around the centre and fails in the outer regions. The two mosaics were divided to give the signal-to-noise ratio, and the result multiplied by the central value of the sensitivity map in order to recover units of mJy beam^{-1}. In order to avoid loss of signal-to-noise ratio in the overlapping regions, and taking into account that the synthesized beams of the nine inner pointings have similar shapes and orientations, the CLEAN mechanism (i.e. the deconvolution of the synthesized beam) has been applied directly to the mosaic, instead of to the individual pointings. To this end, we used the synthesized beam corresponding to the central pointing CrB-B. We placed CLEAN boxes around the strongest features, and CLEANed down to a depth of $2\sigma_{\rm n}$. In the case of the non-source-subtracted mosaics, CLEAN boxes were also placed around the identified radio sources. The same method was applied to the CLEAN map corresponding to pointing CrB-F. In the case of the CrB-G map, as the signal-to-noise ratio is lower and it is not easy to disentangle the real features from the artefacts, we placed a CLEAN box around the region encompassing the primary beam FWHM, and CLEAN was applied down to a depth of $3\sigma_{\rm n}$ in this case.

The CLEANed mosaics, before and after source subtraction, are shown in Fig. 2. In Fig. 3 we present a larger-scale plot of the regions of interest of the CLEANed and source-subtracted mosaic. The maps resulting from the individual pointings CrB-F and CrB-G are shown in Fig. 4. The sensitivity values obtained in each individual pointing are shown in Table 2, and the noise level of the overall mosaic is 12 mJy beam^{-1}.

4 RESULTS AND DISCUSSION

4.1 SZ effect from known clusters in the CrB region

In Table 1 we show the basic data of the eight clusters belonging to the CrB-SC. The X-ray luminosity and electron temperature are given for the four clusters included in the BCS catalogue (Ebeling et al. 1998, 2000); we have also included the more distant clusters A2069 and A2073, for which there are also data in BCS. Since we do not have information on the β parameter [which describes the slope of the density profile in a β-model (Cavaliere & Fusco-Femiano 1976)] and the core radius from X-rays, we have used the relation given by Hernández-Monteagudo & Rubiño-Martín (2004) in terms of the X-ray luminosity ($L_{\rm X}$),

$$\Delta T_{\rm SZ}^{\rm RJ} = -(0.24 \pm 0.06)\left[\frac{L_{\rm X}^{(0.1\text{–}2.4\,{\rm keV})}}{10^{44}\,h_{50}^{-2}\,{\rm erg\,s^{-1}}}\right]^{0.47\pm0.09} {\rm mK}, \qquad (2)$$

in order to make an estimate of the expected central SZ decrement at the VSA frequency

$$(\Delta T_{\rm SZ})_0 = -42.545\,\mu{\rm K}\left(\frac{T_{\rm e}}{\rm keV}\right)\left(\frac{n_{\rm e0}}{10^{-3}\,{\rm cm^{-3}}}\right)\left(\frac{r_{\rm c}}{\rm Mpc}\right) \times \int \left[1+(r/r_{\rm c})^2\right]^{-3\beta/2} {\rm d}(r/r_{\rm c}), \qquad (3)$$

where $T_{\rm e}$ is the electron temperature, $n_{\rm e0}$ the central electron density and $r_{\rm c}$ the core radius.

Making use of the assumption that the intercluster medium (ICM) is a perfect monatomic gas in thermal equilibrium, it follows that the temperature is proportional to $M^{\alpha}(1+z)$, with $\alpha = 2/3$, while the core radius is proportional to $M^{-1/6}(1+z)^{-1/4}$. Hence, we can obtain a scaling relation of the type

$$r_{\rm c} = r_{\rm c0} M_0^{-1/6} (T_{\rm e}/T_{\rm e0})^{-1/4},$$

where

$$T_{\rm e0} = 10^8\,K\,,\; M_0 = 10^{15}\,{\rm M}_{\odot}$$

and $r_{\rm c0} = 0.13\,h^{-1}$ Mpc (Markevitch et al. 1998). These have been used to obtain a rough estimate of the core radius of each of the clusters for which we have X-ray information. To convert to angular sizes, a cosmology $\Omega_{\rm M} = 0.25$, $\Omega_{\Lambda} = 0.75$, $h = 0.73$, as derived from the last VSA results (Rebolo et al. 2004), was used. Making use of these values, and assuming $\beta = 2/3$, we can simulate the response of the VSA to each of these six clusters for which we have X-ray information. The brightness temperature map is converted into flux density, multiplied by the VSA primary beam response, and Fourier-transformed to obtain the simulated aperture-plane response of the VSA to the SZ decrement. We must also consider the primary beam attenuation for clusters displaced from the pointing position. The cluster profiles in the aperture plane for the different observing

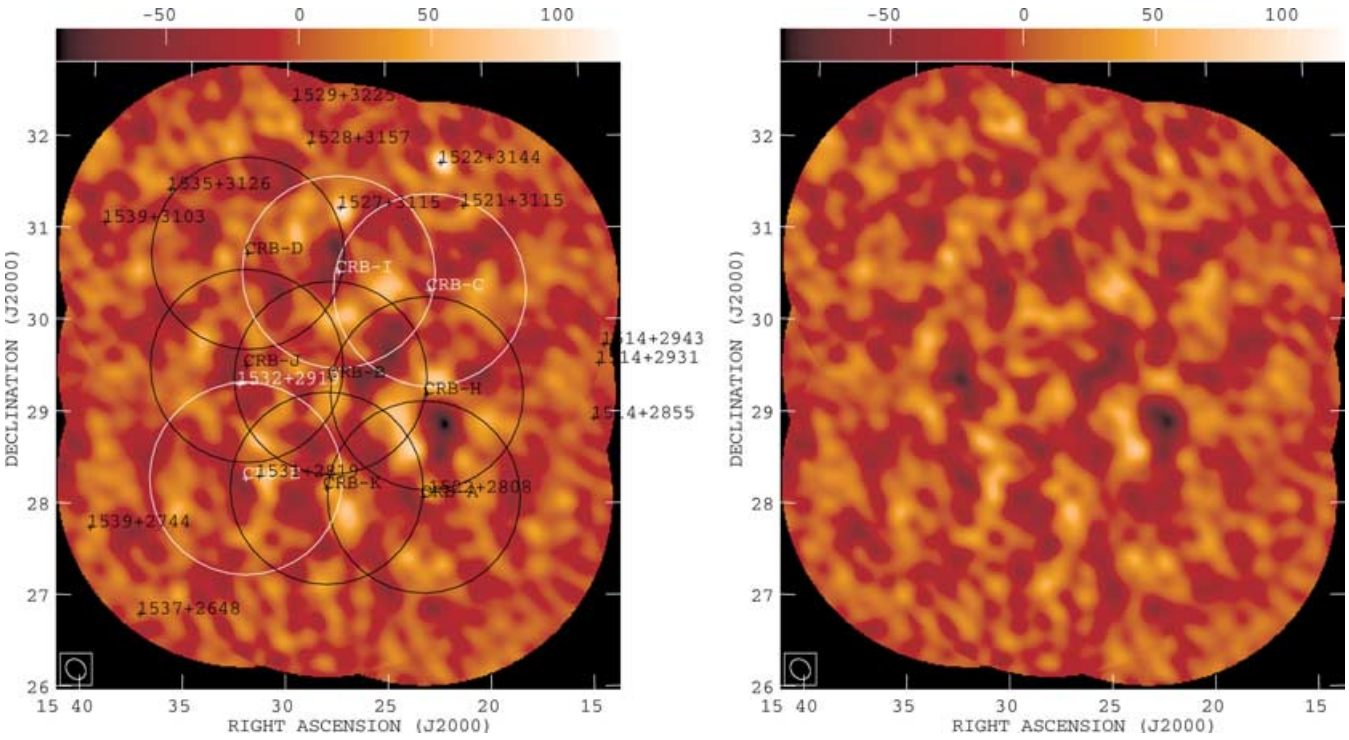

Figure 2. The CLEANed VSA mosaics built up from pointings CrB-A, B, C, D, E, H, I, J and K. In the non-source-subtracted mosaic (left panel) the circles indicate the primary beam FWHM (2.1°) of the nine pointings, and the crosses the positions of the monitored sources with measured fluxes above 50 mJy. The right panel shows the CLEANed source-subtracted mosaic. The synthesized beam FWHM is shown in the bottom left corner (≈11 arcmin). The noise level is practically uniform across the mosaic at a level ≈12 mJy beam^{-1}.

baselines are shown in Fig. 5. It is worthwhile comparing this plot with that presented in the VSA SZ work (Lancaster et al. 2005), which shows profiles with a higher amplitude, and similar shapes. Since, in that study, over a selected sample of rich Abell clusters and with similar noise levels, VSA data have shown clear SZ detections in five out of the seven observed clusters, we do not expect a high-significance detection of SZ effect from the single clusters in the CrB-SC region. Moreover, in this case the decrements are affected by the primary beam response, except in clusters A2019 and A2124, in which the pointing centres and cluster coordinates coincide.

On the other hand, the simulated visibilities for each cluster, computed as explained above, were convolved with the synthesized beam of the closest observation in order to measure the central flux decrements expected in the maps. These values are shown in Table 1 under the symbol $\Delta S_\nu^{\rm pred}$. If we compare the values with the uncertainty in our measurements, we expect to have SZ decrements from single clusters in the region typically with a confidence level between 1σ and 2σ, where σ includes now the contributions from primordial CMB ($\sigma_{\rm CMB} \approx 19$ mJy beam^{-1}), thermal noise ($\sigma_{\rm n}$) and residual sources ($\sigma_{\rm sour} \approx 6$ mJy beam^{-1}). This is exactly what we obtain: comparing the cluster flux values from the final maps (see last column in Table 1), we find excellent agreement for those clusters that have a prediction for the flux. In all 10 clusters analysed, we get negative flux values, and in the two most luminous clusters in the CrB-SC region, A2061 and A2065, we have 2σ detections. These two clusters are located close to larger decrements (see Fig. 3). Moreover, according to Fig. 1, A2065 is located in the region with the highest projected galaxy density. We can now combine all these individual measurements to obtain a statistical detection -24.4 ± 9.2 mJy beam^{-1} (2.7σ). If we also include in this weighted mean those values from A2069 and A2073, we find -24.8 ± 8.1 mJy beam^{-1} (3.0σ), for all the Abell clusters listed in Table 1.

Finally, another point worth noting is the presence of a $5\sigma_{\rm n}$ (signal-to-noise ratio level) decrement (decrement I, see Fig. 3) inside pointing CrB-I, located in a region with a large concentration of galaxy clusters, including A2089 and several Zwicky clusters. Their individual SZ effects could have an important contribution to its total decrement.

4.2 The origin of the negative spots

The most remarkable feature of the mosaic is the existence of two prominent negative spots, at signal-to-noise ratio levels of 6 and 10, situated inside the primary beam FWHM of pointings CrB-B and CrB-H, respectively. Both decrements are extended; indeed, they cover an area equivalent to ≈3 VSA synthesized beams. Coordinates, maximum negative flux densities and brightness temperatures of these strong decrements are listed in Table 4. To convert the flux densities into brightness temperatures, we have used the Rayleigh–Jeans expression

$$T_{\rm RJ} = \frac{\lambda^2}{2k_{\rm B}\Omega_{\rm sb}} S, \qquad (4)$$

where λ is the observing frequency, $k_{\rm B}$ is the Boltzmann constant, and $\Omega_{\rm sb}$ is the solid angle subtended by the synthesized beam.

These decrements are located in regions with no known clusters of galaxies (see Fig. 3). Decrement B is located near the centre of the supercluster, and slightly towards the north is the more distant Abell cluster A2069, which Small et al. (1998) have considered as

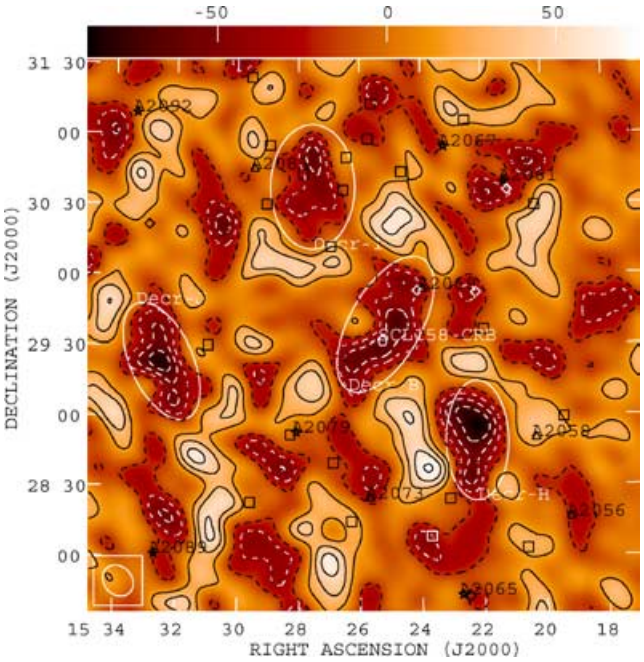

Figure 3. The central region of the CLEANed source-subtracted mosaic shown in the right panel of Fig. 2. We indicate the locations of the four negative decrements. We also show the positions of the clusters extracted from the NASA Extragalactic Database. Five-pointed stars are used for the CrB-SC clusters, triangles for the other Abell clusters, squares for the Zwicky clusters, and diamonds for the clusters present in other catalogues. The centre of the supercluster is indicated with a pentagon. Solid contours show positive flux values, while dashed contours show negative flux values, where all contours correspond to $1.5\sigma_{\rm n}$.

a possible supercluster because of the large number of galaxies it contains. Decrement I and another negative feature (decrement J) located towards the east of the mosaic, inside pointing CrB-J, have similar flux densities to that of decrement B, but with a lower significance (signal-to-noise ratio of 5 in both cases). Note that this latter feature is located in the same position as the radio source 1532+2919, so the error bar of its measured flux (51 ± 12 mJy, see Table 3) may introduce an additional uncertainty.

We searched for possible negative features in the *WMAP* maps (Bennett et al. 2003) in the region of the most intense decrement. Given the angular resolution of the VSA extended configuration, we selected the *WMAP* *W*-band (94 GHz, FWHM $= 0.21^\circ$) map. From this, we can predict the observed visibilities as seen by the VSA, enabling us to build a 'dirty' map. Given the sensitivity of the *WMAP* map ($\approx$170 μK per 7 arcmin pixel in this region, so the corresponding error would be $\approx$108 μK in a VSA synthesized beam of 11 arcmin), we expect to see decrement H only marginally at the $2\sigma_{\rm n}$ level. In the processed *W*-band map we do indeed see a negative spot in the region of decrement H in which the minimum temperature value, $\approx -146 \pm 108$ μK, is located at $15^{\rm h}21^{\rm m}19^{\rm s}$, $+28^\circ55'27''$ (J2000). Note that, although there is an offset of the observed centres of the spots between the VSA and *WMAP* of $\approx$10 arcmin, this is consistent with the instrumental resolutions. Given the noise levels involved, we cannot conclude anything about the nature of the decrement, i.e. we cannot disentangle at $1\sigma_{\rm n}$ level whether the spectrum between 33 and 94 GHz corresponds to primordial CMB (the decrement should have temperature -230 μK at 94 GHz in this case) or to SZ decrement (in which case the signal should have a temperature -185 μK at 94 GHz).

In principle, decrements B and H, given their sizes and amplitudes, could be either extraordinarily large primordial CMB spots, or SZ signals related to either unknown clusters or to diffuse extended warm/hot gas in the supercluster. It should be noted that only one-third of the galaxies in the CrB region are linked to clusters, so SZ contributions could be expected in places where there are no catalogued clusters. As shown in Figs 1 and 3, there are few known galaxies around decrement H, while decrement B is close to a large concentration. This is important since the position of galaxies could trace the warm/hot gas distribution (see, for example, Hernández-Monteagudo et al. 2004). In the next subsections we explore in detail the three possible explanations for the observed decrements.

4.2.1 CMB anisotropy

In order to quantify the possible contribution from the primordial CMB to these large spots, we carried out Monte Carlo simulations. Using CMBFAST (Seljak & Zaldarriaga 1996), we generated a CMB power spectrum with a cosmological model defined by the following parameters: $\Omega_{\rm B} = 0.044$, $\Omega_{\rm M} = 0.25$, $\Omega_\Lambda = 0.75$, $h = 0.73$, $\tau = 0.14$, $n_{\rm S} = 0.97$, as derived from the most recent VSA results (Rebolo et al. 2004), plus $T_{\rm CMB} = 2.725$ K, $\Omega_\nu = 0$ (Bennett et al. 2003), and assuming adiabatic initial conditions. For each decrement we used this power spectrum to carry out 5000 simulations of VSA CMB observations, following the procedure explained in section 3.3 of Savage et al. (2004), and using the aperture plane coverage from each pointing CrB-B and CrB-H as templates. Each visibility point contains the CMB and thermal noise contributions, plus the confusion level introduced by the residual radio sources below the subtraction threshold of 50 mJy. Thus $V = V_{\rm CMB} + V_{\rm n} + V_{\rm sour}$, where

$$V_{\rm sour}(\boldsymbol{u}) = \sum_{i=1}^{N_{\rm sour}} S_i \, {\rm e}^{2\pi \boldsymbol{u}\cdot\boldsymbol{x}_i}, \qquad (5)$$

where $\boldsymbol{u}$ is the position vector of each visibility point, and S_i and $\boldsymbol{x}_i$ are the flux and the position vector in the map plane of the ith source. The fluxes S_i are generated using the source count derived from equation (1), yielding a total of $N_{\rm sour} = 894$ sources distributed between 1 and 50 mJy in a region within 2° of each pointing. The positions $\boldsymbol{x}_i$ are randomly and uniformly distributed inside this region.

In the last column of Table 4 we quote the percentage of realizations in which the minimum CMB flux value is below that found in the real map in the two cases in question. According to these results, the probabilities of decrements B and H being caused by primordial CMB (adding the components due to thermal noise and the residual sources) are 37.82 and 0.38 per cent, respectively. Note that here we are considering only the intensity: the angular size of the spots is disregarded. In order to account for this, we have applied Gaussian smoothing (with a FWHM approximately equal to the FWHM of the spots) to both the simulated and the real maps, and in this case the probabilities of the decrements are higher (see also Table 4). Hence, particularly for decrement H, the low probabilities are mainly due to the negative flux density values rather than the corresponding angular sizes.

We calculate the standard deviations of all pixels located within the 2.1° FWHM of the primary beam in the 5000 realizations, in order to estimate the confusion level introduced by the primordial CMB, the thermal noise and the residual sources components added in quadrature

$$\sigma = \sqrt{\sigma^2_{\rm CMB} + \sigma^2_{\rm n} + \sigma^2_{\rm sour}},$$

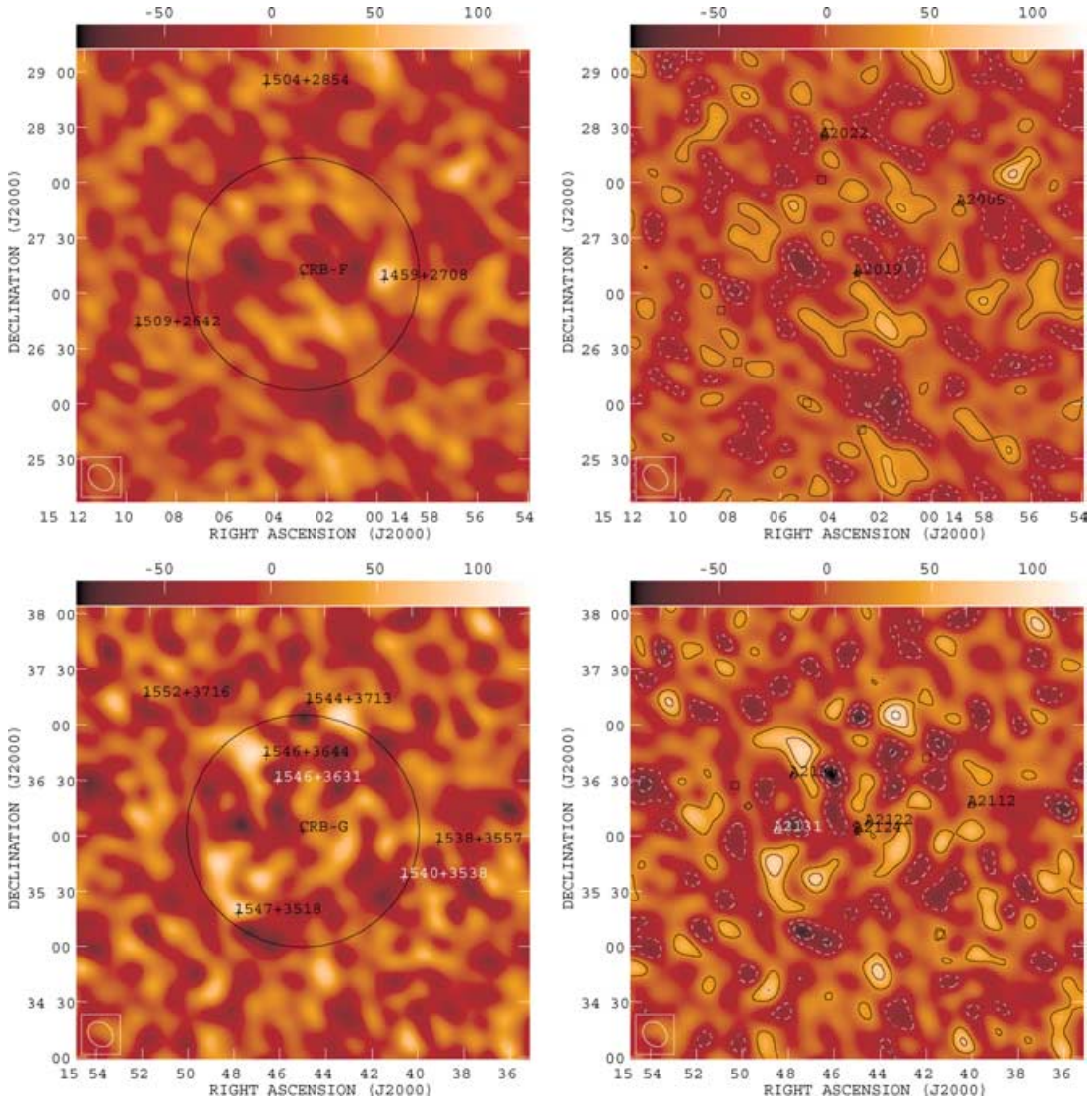

Figure 4. The CLEANed VSA maps corresponding to pointings CrB-F (top panels) and CrB-G (bottom panels). The left column shows the non-source-subtracted maps, while the right column shows the source-subtracted maps. The nomenclature is the same as explained for Figs 2 and 3.

where we have $\sigma_{\rm CMB} \approx 19\,{\rm mJy\,beam^{-1}}$, $\sigma_{\rm n} \approx 11\,{\rm mJy\,beam^{-1}}$ and $\sigma_{\rm sour} \approx 6\,{\rm mJy\,beam^{-1}}$. From this, we find that decrements B and H are deviations at 2.96σ and 4.63σ. These results clearly make a primordial CMB fluctuation alone an unlikely explanation for decrement H. We now focus solely on decrement H.

Following Rubiño-Martín & Sunyaev (2003), we performed a fluctuation analysis. In Fig. 6 we present a logarithmic plot of the histograms, i.e. the $P(D)$ functions, of pixel values from the 5000 realizations and also using the real data from pointing CrB-H. In the case of the realizations, the 1σ error bars (containing the primordial CMB, the thermal noise and the residual sources) are displayed. The plot shows a clear excess in the real data compared with the simulations at flux densities below $\sim -30\,{\rm mJy\,beam^{-1}}$, caused by the presence of decrement H. The excess in the positive tail of the curve comes from the two hot spots located towards the north and the east of decrement H in the final mosaic (see Fig. 3). These positive features could be either real hot spots in the sky or artefacts due to the presence of decrement H itself. (Note also that the response of an interferometer has zero mean, so the presence of a strong negative feature in the map could enhance the neighbouring positive spots.) It may be that these bright spots are enhanced by the presence of radio sources not identified in the extrapolation. However, these positive features are not present in the map of the region constructed using only VSA baselines $>125\lambda$, suggesting that these structures are extended and not point sources. In order to check if these positive spots are due to the sidelobes introduced by decrement H in the convolution with the synthesized beam, we CLEANed the region and find that we obtain lower residuals by placing a CLEAN box around the negative spot than when the CLEAN box is placed around the positive spots. Furthermore, with the box around the negative hole, the intensity of the positive spot is reduced by $\approx$12 per cent. This is clear evidence that these bright spots are enhanced by the sidelobes of the synthesized beam. Using the CLEANed map, the positive tail of the histogram is strongly reduced, while the negative tail is clearly dominant.

We have also computed the power spectrum of the mosaic, following the method described in Scott et al. (2003). This is shown in Fig. 7, along with that obtained from the most recent primordial

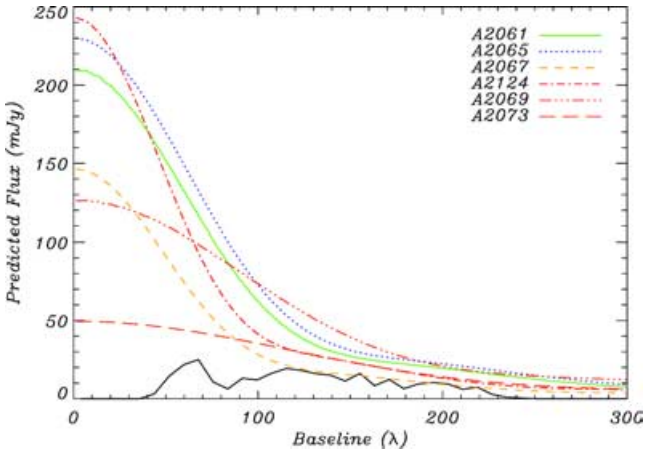

Figure 5. Predicted SZ flux profiles in the aperture plane for four CrB-SC clusters plus two other clusters in the region, as a function of the projected baseline length. The thick solid line represents the VSA weighting function (arbitrary units), computed from these observations.

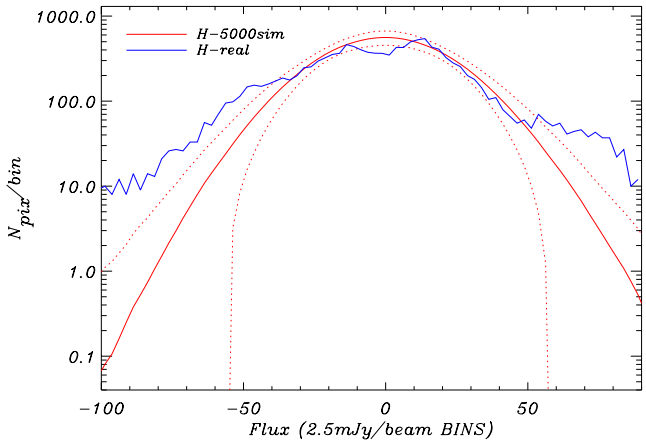

Figure 6. Histograms comparing the distribution of flux densities inside the 2.1° FWHM of the primary beam in the 5000 simulations (lighter curve; red online) and in the real data of pointing CrB-H (dark curve; blue online). We also show the 1σ error bars of the simulations (dotted curve).

CMB observations with the VSA (Dickinson et al. 2004) for comparison. The comparison shows a 2.3σ deviation from the pure primordial CMB behaviour at $\ell \approx 550$. This is as expected, since this scale corresponds to the size of the large decrements. Indeed, we find that, when we compute the power spectrum using data from pointing CrB-H alone, this offset increases to 3.0σ. Moreover, as a consistency check, when we remove pointings CrB-B and CrB-H, which contain decrements B and H, the resulting power spectrum is then compatible with primordial CMB fluctuations on all scales.

4.2.2 *SZ effect from clusters of galaxies*

In order to explore the possible SZ contribution, we followed the formalism utilized by Holder et al. (2000) (see also Kneissl et al. 2001; Battye & Weller 2003) to compute the number of clusters in this region potentially capable of producing a decrement like H. We estimate the mass a cluster would need to have in order to generate an SZ effect at least as intense as a given threshold. In this case the threshold is the amplitude of decrement H, although, to give an idea of the total number of clusters that would be detected in the region, we also considered the confusion level introduced by the quadrature sum of the primordial CMB, the thermal noise and the residual sources ($\sigma \approx 23\,\mathrm{mJy\,beam^{-1}}$). We then calculate the number of clusters per unit redshift in the Universe with masses above this in a solid angle equal to the entire surveyed region ($\approx$24 deg^2), by using the Press & Schechter (1974) (PS) mass function and also the Sheth & Tormen (1999) (ST) mass function, as this provides a better fit to the simulations (note however that simulations also omit much physics). We have adopted $f_{\mathrm{gas}} = 0.12$ (Mohr, Mathiesen & Evrard 1999) for the gas mass fraction of the cluster, $\delta_{\mathrm{c}} = 1.69$ (Peebles 1980) for the critical overdensity, $\sigma_8 = 0.84$ (Bennett et al. 2003) for the spectrum variance in spheres of radius $8\,h^{-1}$ Mpc, and the same values as stated above for the other cosmological parameters.

Fig. 8 shows the derived threshold mass and the number of clusters per unit redshift versus redshift. By integrating this last curve, we obtain the total number of expected clusters in the surveyed region, which is presented in Table 5. The number of SZ clusters that should be detected above the confusion level introduced by the primordial CMB, the thermal noise and the residual sources in the whole surveyed region is three and five, respectively, for the PS and the ST mass functions. They should be located at mean redshifts 0.049 or 0.091, which is close to the mean redshift of the CrB-SC ($\approx$0.07). Note that in our maps we have detected three clusters in the region above this confusion level (see Table 1). On the other hand, the number of clusters that could produce a decrement at least as intense as H is only 0.3 or 0.4, respectively, for the PS and the ST prescriptions. Therefore, the probability of decrement H of being caused entirely by a single cluster is very low. However, if we take into account that a decrement such as H due to SZ may be enhanced by the primordial CMB, this probability must be higher. Note finally that these statistics are valid only for a *random* patch of sky. As we are observing a selected overdense region in the direction of a supercluster, the actual probabilities *must* be higher. To obtain a more precise result, we may turn to N-body simulations, although our analysis is sufficient to get an order-of-magnitude estimation, and to show that these probabilities are low.

4.2.3 *Diffuse extended warm/hot gas*

As indicated in Section 1, superclusters may be reservoirs of diffuse warm/hot gas, which in principle might produce a detectable imprint in the low-energy X-ray bands. Zappacosta et al. (2002), and more recently Zappacosta et al. (2005), have claimed an

Table 4. Coordinates, flux densities and temperatures of the two largest decrements found in the mosaic. We quote both the thermal noise (σ_{n}) and, within parentheses, the quadrature of the primordial CMB, thermal noise and residual sources [$(\sigma^2_{\mathrm{CMB}} + \sigma^2_{\mathrm{n}} + \sigma^2_{\mathrm{sour}})^{1/2}$] error bars. The last column indicates the percentage over the 5000 simulations with minima under each decrement flux density (within parentheses, we also show this value when we apply a smoothing to the data; see Section 4.2.1 for details).

	RA (J2000)	Dec. (J2000)	ΔS_ν (mJy beam^{-1})	ΔT_{RJ} (μK)	Percentage below ΔS_ν
Decrement B	15 25 21.60	+29 32 40.7	-70 ± 12 ($\pm$24)	-157 ± 27 ($\pm$53)	37.82 (54.16)
Decrement H	15 22 11.47	+28 54 06.2	-103 ± 10 ($\pm$22)	-230 ± 23 ($\pm$49)	0.38 (0.72)

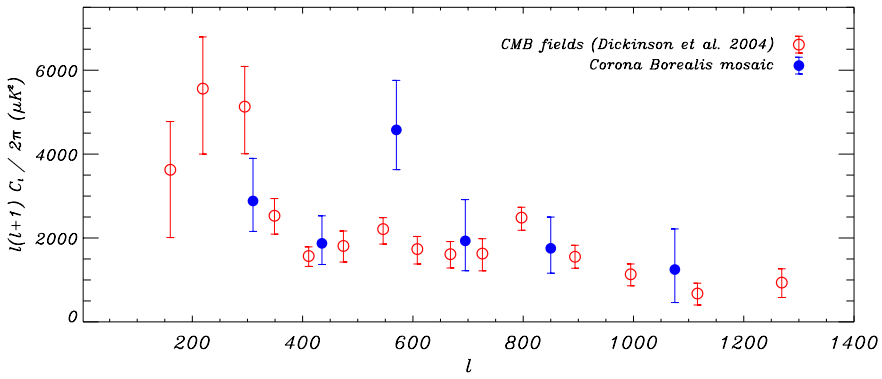

Figure 7. Power spectrum computed from the CrB mosaic (blue online), in comparison with that obtained from the most recent VSA observations of primordial CMB fields (Dickinson et al. 2004; red online). The deviation at $\ell \approx 550$ is due to the presence of decrements B and H (see Section 4.2.1 for details).

excess of X-ray emission from diffuse structures in a high Galactic latitude *ROSAT* field, and the detection of a significant correlation between the *ROSAT*-PSPC pointings and the Münster Redshift Survey of galaxies in the Sculptor supercluster region. The SZ effect may provide another tool to detect this gas, thanks to the long path-lengths of the photons across these large-scale structures. Using the *COBE*-DMR data, Molnar & Birkinshaw (1998) were unable to find evidence of an SZ imprint in the region of the Shapley supercluster.

Since decrement B, according to our studies, can be explained through a primordial CMB decrement, we shall focus on decrement H, and explore whether it could have been built up from a concentration of diffuse warm/hot gas ($T_e < 1$ keV). Such a structure producing a detectable SZ effect could also leave an imprint on the less energetic X-ray bands. We have analysed the *ROSAT* XRT/PSPC All-Sky Survey (Snowden et al. 1997) map, corresponding to the R6 band (0.73–1.56 keV), in order to search for correlated X-ray diffuse emission in the region. The R6 map does not show an excess of emission in the position of the decrement (see Fig. 9). The signal in the region of the decrement is $\sim$(80–140) $\times$ 10^{-6} count s^{-1} arcmin^{-2}, which comes mainly from the background. In order to perform the *ROSAT*–VSA correlation, we have adopted two different methods.

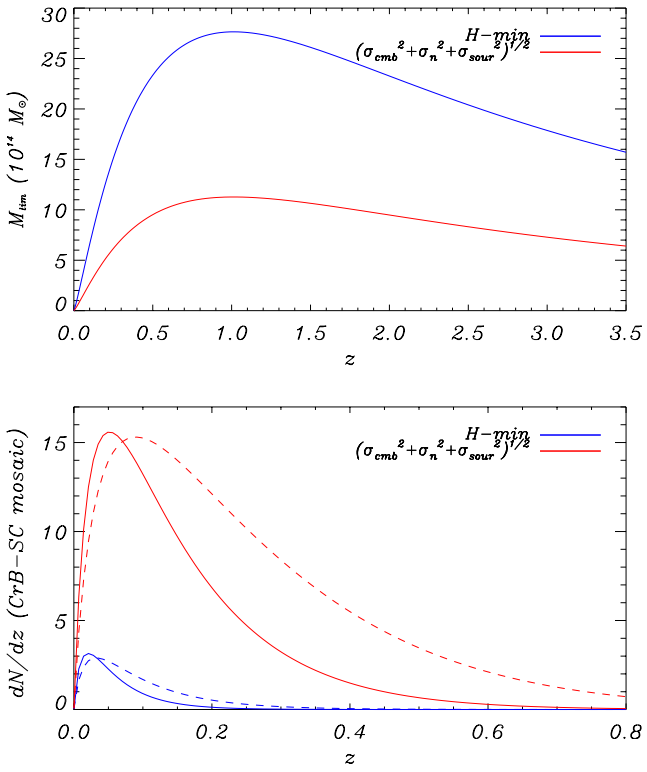

Figure 8. Minimum SZ effect detectable mass versus redshift (top) and number of expected clusters per redshift unit versus redshift (bottom), using as thresholds either the sum in quadrature of the standard deviations of the primordial CMB, the thermal noise and the residual sources (lighter curve; red online), and the flux density of spot H (dark curve; blue online). The solid and dashed lines correspond respectively to the PS and ST mass functions.

First, we have applied a pixel-to-pixel comparison of the *ROSAT*-R6 map and the real-space CLEANed mosaic following the method described in Hernández-Monteagudo & Rubiño-Martín (2004). This method considers the brightness temperature measured by a CMB experiment such as the VSA as the sum of different components: a cosmological signal $T_{\rm CMB}$, the template we want to measure M (in this case, the thermal SZ component traced by *ROSAT*), instrumental noise N, and foreground residuals F. The total signal measured at a given position on the sky is then modelled as $T = T_{\rm CMB} + \alpha M + N + F$, where α measures the amplitude of the template induced signal. If all the other components have zero mean and well-known correlation functions, and $\mathcal{C}$ denotes the correlation matrix of the CMB and noise components, then the estimate of α and its statistical error are

$$\alpha = \frac{T\mathcal{C}^{-1}M^{\rm T}}{M\mathcal{C}^{-1}M^{\rm T}}, \qquad \sigma_\alpha = \sqrt{\frac{1}{M\mathcal{C}^{-1}M^{\rm T}}}. \tag{6}$$

The derived value of the correlation between *ROSAT* and the VSA mosaic is $\alpha = -0.28 \pm 0.74$ μK/X (X denotes the units of the R6 map, which are count s^{-1} arcmin^{-2}), which means that there is no significant anticorrelation, as would be expected if it were the case that the decrement is produced by a diffuse gas distribution.

We repeated this analysis, but in visibility space, by predicting the expected visibilities from the *ROSAT* map as seen by the VSA, and performing a similar comparison between the observed and predicted values. In this case, we find $\alpha = -0.21 \pm 0.57$ μK/X for the CrB-H field. The significance of this value was derived by computing the dispersion of the α value when performing a series of rotations of one map with respect to the other prior to the computation of the predicted visibilities.

Assuming the distance of the supercluster ($\approx 200\,h^{-1}$ Mpc, derived from the average redshift of the member clusters $\langle z \rangle = 0.0725$), the physical transverse size of decrement H is $\approx 2\,h^{-1}$ Mpc. At typical WHIM electron temperatures, i.e. $T_e = 0.01$ to 1 keV, a homogeneous and spherical gas distribution of this size producing a central

Table 5. Maximum threshold masses, their redshifts, number of detectable clusters in the whole survey, and the most likely redshift for clusters producing an SZ effect larger than either the confusion level introduced by the primordial CMB, the thermal noise and the residual sources and the minimum flux density of pointing H. We have used both the PS and the ST mass functions.

Threshold	Maximum $M_{\rm lim}$ ($10^{14}\,{\rm M}_\odot$)	z where $M_{\rm lim}$ is maximum	Total number of clusters		$z\,{\rm d}N/{\rm d}z$ is maximum	
			PS	ST	PS	ST
$\lvert$H-min$\rvert = 103\,{\rm mJy\,beam^{-1}}$	27.65	1.01	0.3	0.4	0.021	0.035
$\sqrt{\sigma^2_{\rm CMB}+\sigma^2_{\rm n}+\sigma^2_{\rm sour}} \approx 23\,{\rm mJy\,beam^{-1}}$	11.27	1.01	3.2	5.4	0.049	0.091

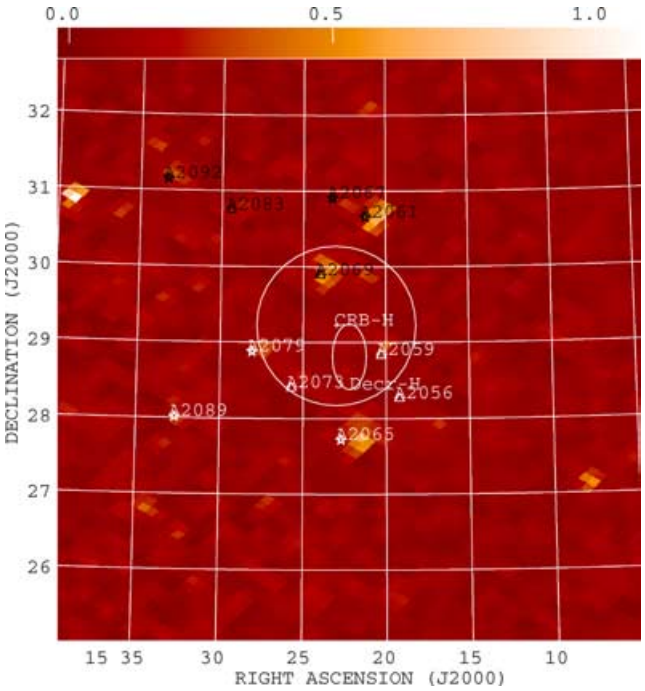

Figure 9. The *ROSAT*-R6 (0.73–1.56 keV) (Snowden et al. 1997) map centred on pointing CrB-H. We indicate the positions of all the Abell clusters in the region, emphasizing the CrB-SC clusters with a star. The units indicated in the upper flux bar are 10^{-3} count s^{-1} arcmin^{-2}. The circle indicates the FWHM of the primary beam of pointing CrB-H, while the ellipse corresponds to the position of decrement H in the VSA mosaic. There is no clear excess of emission in this region.

SZ decrement of 230 μK would have such a high $n_{\rm e}$ that it must have collapsed, with subsequent virialization. This should also produce detectable X-ray emission, which is not present in the *ROSAT*-R6 map. In a similar case of a CMB decrement without X-ray emission, Kneissl, Sunyaev & White (1998) discuss various possibilities, but find it difficult to reconcile observations with the process of structure formation. A filament pointing towards us seems in some ways one of the more attractive options. We may therefore consider a larger structure with a lower density so that the path-length is long enough to produce a detectable SZ effect ($\Delta T_{\rm SZ} \propto \int n_{\rm e} T_{\rm e}\,{\rm d}l$) without significant X-ray emission ($S_{\rm X\text{-}ray} \propto \int n_{\rm e}^2 T_{\rm e}^{1/2}\,{\rm d}l$). We can estimate the peak SZ intensity caused by this hypothetical filamentary structure aligned along the line of sight, with a depth L, a central electron density $n_{\rm e}$, and electron temperature $T_{\rm e}$, at the VSA frequency of 33 GHz:

$$\Delta T_0 f = -21.3\,\mu{\rm K}\left(\frac{L}{\rm Mpc}\right)\left(\frac{n_{\rm e}}{10^{-3}\,{\rm cm^{-3}}}\right)\left(\frac{T_{\rm e}}{\rm keV}\right). \quad (7)$$

Here, $\Delta T_0 = 230\,\mu$K is the peak SZ decrement. Given that there could also be a contribution from primordial CMB anisotropies, we have introduced the factor f, which accounts for the fraction of the decrement due to the SZ effect. For simplicity, we have assumed isothermality and that the electron density is homogeneous along the line of sight. We have assumed that the depth of this structure must be lower than the maximum separation along the line of sight between clusters in the core of the CrB-SC, which is $29\,h^{-1}$ Mpc $= 40$ Mpc. These assumptions set constraints on the overdensity (expressed by the baryon density over the universal mean baryon density) and $T_{\rm e}$, which are represented in Fig. 10 by the dashed ($L < 40$ Mpc) and the dotted lines ($L < 20$ Mpc).

We also require the bremsstrahlung emission to be low enough that the signal does not leave a detectable imprint on the *ROSAT*-R6 map. We use equation (7) to derive a relation between L and $T_{\rm e}$, and integrate along the line of sight. We consider a background level of 10^{-4} count s^{-1} arcmin^{-2} (see Fig. 9) as an upper limit for the X-ray emission in the region of decrement H. Scaling with the signal of the Coma cluster in the same band (63×10^{-4} count s^{-1} arcmin^{-2}), we obtain the constraint represented by the solid line of Fig. 10. Filled zones in the parameter space show the acceptability regions for structures with lengths of less than 40 Mpc. These plots show that for $f = 1$ there is no reasonable combination of $n_{\rm e}$ and $T_{\rm e}$ to explain the whole decrement. Only values of $f \lesssim 0.7$ are able to explain the decrement. For instance, a filament with a temperature $T_{\rm e} \approx 0.7$ keV, a depth $L \approx 40$ Mpc and a baryon overdensity $\delta\rho_{\rm B}/\langle\rho_{\rm B}\rangle \approx 850$ would produce an X-ray signal of $\approx 0.6 \times 10^{-4}$ count s^{-1} arcmin^{-2}, which is almost a factor of 2 below the background confusion level of the *ROSAT*-R6 map. A structure having these parameters would also produce a peak SZ effect of $\approx 115\,\mu$K, which is half of the amplitude of the decrement ($f = 0.5$). Also, a remarkable *alignment* is required to achieve this fraction of brightness contrast.

If, instead of the value $\delta\rho_{\rm B}/\langle\rho_{\rm B}\rangle \approx 850$, which is computed for the centre of the filament, we assume an average value of $\delta\rho_{\rm B}/\langle\rho_{\rm B}\rangle \approx 450$ over the entire structure, and a 2×2 Mpc^2 square for the transverse shape of the filament, the total gas mass enclosed in it would be $M_{\rm gas} \approx 5 \times 10^{14}\,{\rm M}_\odot$. This overdensity appears to be difficult to explain in the light of current hydrodynamical galaxy formation simulations, which predict overdensities ≈ 10 times lower for these large-scale structures (Cen & Ostriker 1999). If we assume that the dark matter is well traced by the baryonic matter, this leads to an overdensity of ≈ 110 in terms of the total matter, in contrast to the typical values for non-bound supercluster scales with $\delta\rho/\rho_{\rm c} \sim 5$–40, for structures that have just become virialized with $\delta\rho/\rho_{\rm c} \sim 200$, or inside the typical Abell clusters with $\delta\rho/\rho_{\rm c} \sim 1000$. We note that the derived gas mass contained in this hypothetical filament is comparable to the total baryonic mass in the known CrB-SC clusters, and would represent ≈ 10 per cent of the total baryonic mass of the supercluster.

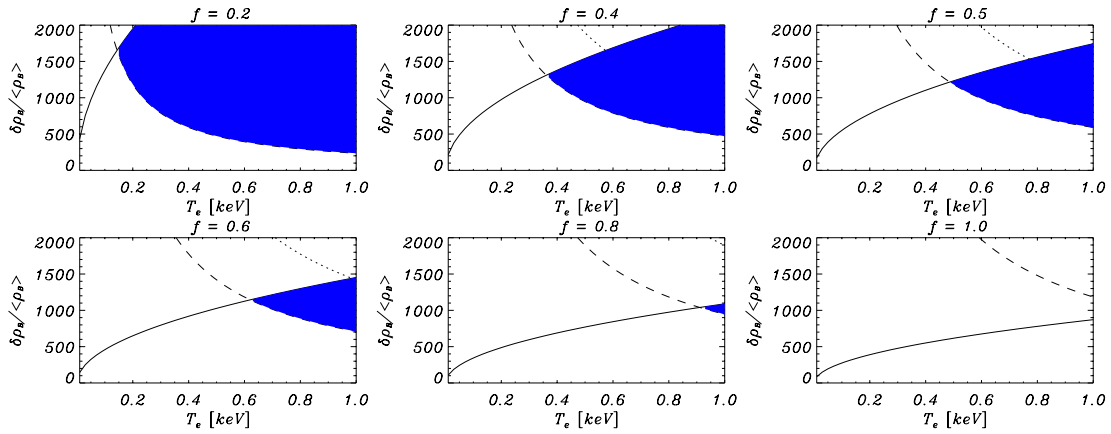

Figure 10. Constraints placed on the overdensity (expressed in terms of baryon density over the mean baryon density) and the electron temperature in the centre of the assumed gas concentration (see Section 4.2.3 for details) that generates decrement H. We take into account that the X-ray emission must be below that in the *ROSAT*-R6 map (solid line), and that the depth of this structure should be lower than 40 Mpc (dashed line), or lower than 20 Mpc (dotted line). Filled regions indicate the acceptable combinations in the parameter space (for 40 Mpc). The factor f represents the fraction of the decrement that is produced by the SZ effect.

5 CONCLUSIONS

We have *selected* the wholly unusual Corona Borealis supercluster region for CMB observations with the VSA extended array at 33 GHz. The structures detected in the mosaicked map of the core of the supercluster have significant contributions from primordial CMB anisotropies. However, these maps show negative flux values at the positions of the 10 richest clusters in the region, and the two most X-ray-luminous CrB-SC clusters, A2061 and A2065, each produce 2σ decrements. When we combine the flux values from the positions of the CrB-SC member clusters, we obtain a statistical SZ detection with a significance of 2.7σ (24.4 ± 9.2 mJy beam^{-1}). If the clusters A2069 and A2073, which have higher redshifts, are added to the sample, we obtain 3.0σ (24.8 ± 8.1 mJy beam^{-1}). In addition to this, the mosaic shows, in a region with a high density of Zwicky clusters, a large negative feature, at a signal-to-noise ratio of 5, which could be enhanced by the SZ effects generated by these single clusters.

This mosaic shows two strong and extended negative features with flux densities -70 ± 12 mJy beam^{-1} (-157 ± 27 μK) and -103 ± 10 mJy beam^{-1} (-230 ± 23 μK), and positions $15^{\rm h}25^{\rm m}21\overset{\rm s}{.}60$, $+29^{\circ}32'40.7''$ (J2000) and $15^{\rm h}22^{\rm m}11\overset{\rm s}{.}47$, $+28^{\circ}54'06.2''$ (J2000), respectively. These decrements are located at positions where there are no known clusters. The first one is placed near the reported centre of the supercluster. In order to disentangle their origins, we have considered the possibility of large primordial CMB fluctuations, or SZ signals related to either unknown clusters or to diffuse extended warm/hot gas in the intergalactic medium of the supercluster. The primordial contribution has been explored by performing simulations of primordial CMB observations with the VSA. These have shown that the size and intensity of decrement B are consistent with primordial CMB fluctuations, whereas in the case of decrement H the probability is only 0.38 per cent. Decrement H is marginally detected in the *W*-band map of the *WMAP* first-year data set, but the current sensitivity does not allow us to disentangle the spectral behaviour of this decrement.

In order to investigate the second possibility, we have predicted the number of clusters capable of producing a decrement such as H. To this end we used the Press–Schechter (PS) and also the improved Sheth–Tormen (ST) prescriptions to describe the density of collapsed objects in the Universe. This study showed that the number of random clusters in the VSA observed fields massive enough to produce this feature is 0.3 and 0.4, respectively, for the PS and the ST formalisms. Note that this probability has been computed assuming that the whole decrement is due to the SZ effect. If we take into account that there could be a primordial CMB contribution, this probability becomes higher.

The *ROSAT*-R6 data show no evidence of X-ray emission in the region of decrement H. This fact sets constraints on the electron density and temperature that could have a hypothetical intercluster warm/hot gas distribution capable of producing a decrement as deep as H. If it were in a small volume, then the electron density would be high enough to produce detectable X-ray emission in the typical ranges of WHIM temperatures (0.01–1 keV). Hence, we hypothesize that the decrement could be caused by a large filament aligned in the direction of our line of sight. We have explored the possibility that only some fraction of the spot is due to an SZ effect, the primordial CMB being responsible for the rest. In this case, a filament with a length below the size of the supercluster, i.e. $\lesssim$40 Mpc, a temperature of 0.5–0.8 keV, and a baryon density in its centre between 500 and 900 times the mean baryon density in the Local Universe produces an SZ effect close to one-half the central flux density of the decrement, and its X-ray emission would be low and obscured by the background in the *ROSAT*-R6 map. It would contain a gas mass of $\sim 5 \times 10^{14}\,{\rm M}_{\odot}$, which is comparable to the total baryonic mass contained in the CrB-SC member clusters. If the value $3 \times 10^{16}\,{\rm M}_{\odot}$ is assumed for the total mass of the supercluster, this filament would hold the $\sim$10 per cent of the total expected baryonic mass of the supercluster. However, the required overdensity of such structure is $\sim$10 times higher than the predictions from *N*-body galaxy formation simulations for these large-scale filaments. However, we stress that: (i) we are observing at a very atypical region, and (ii) *N*-body simulations need more physics.

In summary, we are confident that our measurements do show excess decrement, and to explain decrement H we require a combination of primordial CMB fluctuations with an SZ effect either from an unknown cluster or from a large-scale filamentary structure, which would hold a significant fraction of the total baryonic mass of the supercluster. It is worthwhile to carry out

multifrequency observations of decrement H in order to disentangle these possibilities.

ACKNOWLEDGMENTS

We thank the staff of the Teide Observatory, Mullard Radio Astronomy Observatory and Jodrell Bank Observatory for assistance in the day-to-day operation of the VSA. We thank PPARC for funding and supporting the VSA project. Partial financial support was provided by the Spanish Ministry of Science and Technology project AYA2001-1657. We acknowledge E. S. Battistelli, F. Atrio-Barandela and J. Betancort-Rijo for useful comments and discussions. CD is funded by a Stanley Rawn post-doctoral scholarship. We acknowledge the use of the NASA/IPAC Extragalactic Database (NED), operated by JPL (Caltech), under contract with NASA. We also acknowledge the use of the AIPS package, developed by the NRAO.

REFERENCES

Abell G. O., 1958, ApJS, 3, 211
Banday A. J., Gorski K. M., Bennett C. L., Hinshaw G., Kogut A., Smoot G. F., 1996, ApJ, 468, L85
Battye R. A., Weller J., 2003, Phys. Rev. D, 68, 083506
Bennett C. L. et al., 2003, ApJS, 148, 1
Birkinshaw M., 1999, Phys. Rep., 310, 97
Briel U. G., Henry J. P., 1995, A&A, 302, L9
Burles S., Nollett K. M., Turner M. S., 2001, ApJ, 552, L1
Cavaliere A., Fusco-Femiano R., 1976, A&A, 49, 137
Cen R., Ostriker J. P., 1999, ApJ, 514, 1
Cleary K. A. et al., 2005, MNRAS, 360, 340
Condon J. J., Cotton W. D., Greisen E. W., Yin Q. F., Perley R. A., Taylor G. B., Broderick J. J., 1998, AJ, 115, 1693
Davé R. et al., 2001, ApJ, 552, 473
Dickinson C. et al., 2004, MNRAS, 353, 732
Ebeling H., Edge A. C., Bohringer H., Allen S. W., Crawford C. S., Fabian A. C., Voges W., Huchra J. P., 1998, MNRAS, 301, 881
Ebeling H., Edge A. C., Allen S. W., Crawford C. S., Fabian A. C., Huchra J. P., 2000, MNRAS, 318, 333
Einasto M., Einasto J., Tago E., Müller V., Andernach H., 2001, AJ, 122, 2222
Finoguenov A., Briel U. G., Henry J. P., 2003, A&A, 410, 777
Fosalba P., Gaztañaga E., Castander F. J., 2003, ApJ, 597, L89
Fukugita M., Hogan C. J., Peebles P. J. E., 1998, ApJ, 503, 518
Grainge K. et al., 2003, MNRAS, 341, L23
Gregory P. C., Scott W. K., Douglas K., Condon J. J., 1996, ApJS, 103, 427
Greisen E., ed., 1994, AIPS Cookbook. NRAO, Green Bank, WV
Hernández-Monteagudo C., Rubiño-Martín J. A., 2004, MNRAS, 347, 403
Hernández-Monteagudo C., Genova-Santos R., Atrio-Barandela F., 2004, ApJ, 613, L89
Holder G. P., Mohr J. J., Carlstrom J. E., Evrard A. E., Leitch E. M., 2000, ApJ, 544, 629
Jarrett T. H., Chester T., Cutri R., Schneider S. E., Huchra J. P., 2003, AJ, 125, 525
Kneissl R., Sunyaev R. A., White S. D. M., 1998, MNRAS, 297, L29
Kneissl R., Jones M. E., Saunders R., Eke V. R., Lasenby A. N., Grainge K., Cotter G., 2001, MNRAS, 328, 783
Lancaster K. et al., 2005, MNRAS, 359, 16
Marini F. et al., 2004, MNRAS, 353, 1219
Markevitch M., Forman W. R., Sarazin C. L., Vikhlinin A., 1998, ApJ, 503, 77
Mason B. S., Leitch E. M., Myers S. T., Cartwright J. K., Readhead A. C. S., 1999, AJ, 118, 2908
Mohr J. J., Mathiesen B., Evrard A. E., 1999, ApJ, 517, 627
Molnar S. M., Birkinshaw M., 1998, ApJ, 497, 1
Myers A. D., Shanks T., Outram P. J., Frith W. J., Wolfendale A. W., 2004, MNRAS, 347, L67
Page L. et al., 2003, ApJS, 148, 233
Peebles P., 1980, The Large-Scale Structure of the Universe. Princeton Univ. Press Princeton NJ
Postman M., Geller M. J., Huchra J. P., 1988, AJ, 95, 267
Press W. H., Schechter P., 1974, ApJ, 187, 425 (PS)
Rauch M. et al., 1997, ApJ, 489, 7
Rebolo R. et al., 2004, MNRAS, 353, 747
Rubiño-Martín J. A., Sunyaev R. A., 2003, MNRAS, 344, 1155
Savage R. et al., 2004, MNRAS, 349, 973
Scharf C., Donahue M., Voit G. M., Rosati P., Postman M., 2000, ApJ, 528, L73
Scott P. F. et al., 2003, MNRAS, 341, 1076
Seljak U., Zaldarriaga M., 1996, ApJ, 469, 437
Shane C. D., Wirtanen C. A., 1954, AJ, 59, 285
Sheth R. K., Tormen G., 1999, MNRAS, 308, 126 (ST)
Small T. A., Sargent W. L. W., Hamilton D., 1997, ApJS, 111, 1
Small T. A., Ma C., Sargent W. L. W., Hamilton D., 1998, ApJ, 492, 45
Snowden S. L. et al., 1997, ApJ, 485, 125
Sołtan A. M., Freyberg M. J., Hasinger G., 2002, A&A, 395, 475
Spergel D. N. et al., 2003, ApJS, 148, 175
Taylor A. C. et al., 2003, MNRAS, 341, 1066
Tittley E. R., Henriksen M., 2001, ApJ, 563, 673
Watson R. A. et al., 2003, MNRAS, 341, 1057
Zappacosta L., Mannucci F., Maiolino R., Gilli R., Ferrara A., Finoguenov A., Nagar N. M., Axon D. J., 2002, A&A, 394, 7
Zappacosta L., Maiolino R., Mannucci F., Gilli R., Schuecker P., 2005, MNRAS, 357, 929

This paper has been typeset from a TEX/LATEX file prepared by the author.